Article

Treatment of Wastewater Using a Magnetically Recoverable Ag-Based Photocatalyst

J. Jaime Sadhwani Alonso [1,2] , **Jenifer Vaswani Reboso** [1,3,*] and **Dunia E. Santiago** [1,4]

1 Department of Process Engineering, Universidad de Las Palmas de Gran Canaria, Campus de Tafira, 35017 Las Palmas, Spain; jimmy.sadhwani@ulpgc.es (J.J.S.A.); dunia.santiago@ulpgc.es (D.E.S.)

2 Group of Industrial Efficiency, Instrumentation and Protection Systems (Grupo de Sistemas Industriales de Eficiencia, Instrumentación y Protección—SEIP), Universidad de Las Palmas de Gran Canaria, 35017 Las Palmas, Spain

3 Group of Environmental Sources Analytical Control (Grupo Control Analítico de Fuentes Medioambientales—CAFMA), Institute of Environmental Studies and Natural Resources (Instituto de Estudios Ambientales y Recursos Naturales—i-UNAT), Universidad de Las Palmas de Gran Canaria, 35017 Las Palmas, Spain

4 Group of Photocatalysis and Spectroscopy for Environmental Applications (Fotocatálisis y Espectroscopia para Aplicaciones Medioambientales—FEAM), Institute of Environmental Studies and Natural Resources (Instituto de Estudios Ambientales y Recursos Naturales—i-UNAT), Universidad de Las Palmas de Gran Canaria, 35017 Las Palmas, Spain

* Correspondence: jenifer.vaswani@ulpgc.es

Abstract: A novel catalyst, composed of silver phosphate (Ag_3PO_4) deposited on a magnetic material containing titanium dioxide (TiO_2) and ferromagnetite (Fe_3O_4), was synthesized and tested with wastewater from the maintenance system of a swimming pool and from the secondary effluent of a wastewater treatment plant (WWTP). The magnetic material $Ag_3PO_4@1$-TiO_2-Fe_3O_4 presented a slightly lower photoactivity than bare Ag_3PO_4 but was able to remove over 64% COD from the secondary effluent of a WWTP and over 75% organic UV filters from a swimming pool wastewater. The material was easily recovered from the treated water with a magnet and could be reused at least four times. The efficiency loss after five reuses was 15%. The dissolution of silver after the photocatalytic reaction was over 80 $mg \cdot L^{-1}$ for bare Ag_3PO_4 and less than 500 $\mu g \cdot L^{-1}$ for the magnetic composites. The magnetic support prevents the dissolution of silver. The materials that contained Ag_3PO_4 showed antibacterial properties under dark conditions. The photocatalytic efficiency of Ag_3PO_4 and commercial TiO_2 was similar under sunlight, both for the removal of UV filters at $\mu g \cdot L^{-1}$ concentrations from swimming pool wastewater, and for the removal of mild COD loads from a WWTP effluent (initial COD: 110 $mg \cdot L^{-1}$).

Keywords: emerging contaminants; organic UV filters; silver phosphate; ferromagnetite; titanium dioxide; swimming pool wastewater; WWTP effluent

1. Introduction

In recent years, there has been growing concern about the presence of emerging contaminants (ECs) in natural water bodies. These are anthropogenic compounds, like pharmaceuticals or personal care products, among others, that are found in trace concentrations in the environment. These contaminants can reach the water bodies through several pathways, although one of the main ones is the disposal of urban wastewater treatment plant (WWTP) effluents [1].

Conventional WWTPs, normally based on biological treatments, are generally designed to reduce the organic load of wastewater to comply with the legal limit to dispose of

or reuse the treated water. One of the main parameters followed in WWTPs is the chemical oxygen demand (COD). For example, in the European Union (EU), the COD legal limit for wastewater disposal is currently 125 $mg \cdot L^{-1}$ [2]. There is no specific regulation for the disposal of most ECs, although several studies have proven that these compounds, even at low concentrations, can affect human health and reproduction [3], are toxic to aquatic species [4,5], and increase bacterial resistance [6]. Some of the ECs detected in WWTPs, such as some personal care products, are recalcitrant to biodegradation, and end up in the natural water bodies where the effluents of WWTPs are discharged [7]. Such is the concern about the effect that ECs can cause that the EU created in 2013 a watch list of priority substances hazardous to the aquatic environment. This list is updated every two years [8]. In 2022, three UV filters were added to the watch list, namely, butyl methoxydibenzoyl-methane (or avobenzone) (BMDBM), octocrylene (OC), and benzophenone-3, also known as oxybenzone (BP-3) [9]. These UV filters, among others, have been reported to be present in the effluent of several conventional activated sludge-based WWTPs [10], which indicates that the biodegradability of these compounds is in fact low.

The pollutants that present low biodegradability are normally known as recalcitrant molecules. Conventional WWTPs, based on biological methods, are not capable of removing these pollutants, and, thus, other treatments must be employed. Heterogeneous photocatalysis is based on the production of oxidizing and non-specific species, such as hydroxyl radicals ($\cdot$OH), and is a possible alternative for the removal of these recalcitrant pollutants. Titanium dioxide (TiO_2) is the widest employed heterogeneous photocatalyst, although its main drawback is that it needs to be irradiated with ultraviolet (UV) radiation o($\lambda \leq 400$ nm) [11]. This limits the option of using natural sunlight in the photocatalytic process because only about 5% of the solar spectrum meets this limitation; about 45% of the spectrum is in the visible range (400–760 nm) and the rest is infrared [12].

Silver phosphate (Ag_3PO_4) is an alternative photocatalyst that is widely known due to its antibacterial properties [13] and is active under visible light [14]. However, the adsorption of contaminants on this material is hindered by its low specific surface area, which is commonly below 3 $m^2 \cdot g^{-1}$ [15]. Additionally, Ag_3PO_4 is slightly soluble in water (0.02 $g \cdot L^{-1}$) and the dissolved silver ions are reduced to silver atoms (Ag^0) by the photogenerated electrons [16]. This is known as photocorrosion, and, to minimize this effect, electron sacrificial agents must be introduced. In this sense, several authors have modified Ag_3PO_4 with the deposition of precious metals, ion doping techniques, or the coupling of semiconductors.

The coupling of Ag_3PO_4 with graphitic carbon nitride (g-C_3N_4) [17–19] or TiO_2 [20–25] is the most frequently reported technique. The heterojunction formed via the coupling of a semiconductor with a wide bandgap, like TiO_2, with another one with a smaller bandgap, inhibits the recombination of electrons and holes thanks to the transfer of electrons between the two semiconductors [15,26].

The use of Ag_3PO_4 and Ag_3PO_4 composites in photocatalysis has been widely studied for the degradation of target molecules in distilled water. However, to date and to the best of our knowledge, there are only nine previous reports (from a search on Scopus conducted on 23 March 2024) that deal with the use of Ag_3PO_4-based photocatalysts for the treatment of contaminants in a real or industrial wastewater matrix. All of them spike a contaminant in the wastewater and follow the degradation kinetics of that specific molecule [27–32].

For instance, several authors studied the capacity of different Ag_3PO_4-based materials for the removal of tetracyclines, spiked into different water matrices, such as municipal, medical, or swine wastewater, in addition to river or tap water [27–29]. All found that the degradation of the target compound was lower in such water matrices compared to deionized water. Other authors reported the same findings for the study of Ag_3PO_4-

based materials to remove dyes (mainly methylene blue, methyl orange, or rhodamine B) spiked into seawater, pond water, or textile wastewater [30–32]. The inhibition effect in degradation caused by the different water matrices is a consequence of the occurrence of competing species and ions. For instance, chloride is known to scavenge hydroxyl radicals, and, additionally, it can react with Ag_3PO_4 to form AgCl [33].

Another issue in heterogeneous photocatalysis is to find proper support to reduce the cost of the separation and reuse of the photocatalysts from the treated water. However, the immobilization of the catalyst leads to lower reaction rates because the exposed surface area decreases, and the supporting material can interfere with the reaction process [34]. In recent years, the use of magnetic materials to support photocatalysts has attracted special attention because it allows high surface areas to be exposed. In most of the studies conducted in this regard, ferromagnetite (Fe_3O_4) was used as magnetic support [35–40].

To our knowledge, very few previous works have reported the use of Ag_3PO_4/magnetic nanocomposites for photocatalysis. Some authors used other magnetic materials as support for Ag_3PO_4, such as Fe_3O_4 [36], magnetic graphene oxide (GO) [41,42], and spinel ferrites such as manganese ferrite [43], cobalt ferrite [44], or nickel ferrite [45].

However, most previous studies were performed using dyes (mainly methylene blue and Rhodamine B) as probe molecules in distilled water. Some also used bacteria (mainly *E. coli* and *S. aureus*), cultivated in Petri dishes and exposed to the silver-based materials, to determine the antibacterial activity of the materials. In the case of using methylene blue as a probe molecule, recent studies have shown that this dye is unsuitable for photocatalytic testing under visible light due to direct photocatalytic oxidation, as it suffers at 400–500 nm [46]. Thus, studies with other probe molecules are necessary.

Regarding the application of magnetic Ag_3PO_4-based materials for the treatment of real wastewater, to date, there are no previous studies concerning this topic in the literature. We believe that it is fundamental to evaluate the efficiency of these photocatalysts in the treatment of real wastewater to determine whether these materials could be used in industrial applications.

In this work, Ag_3PO_4 was synthesized and supported onto magnetic materials (Fe_3O_4 or TiO_2–Fe_3O_4). Ag_3PO_4 was chosen for its antibacterial properties, in addition to its activity under visible light. TiO_2 was added to the composite for its proven photoactivity. Lastly, Fe_3O_4 was chosen as a magnetic support because of its simplicity and wide use in this respect. The TiO_2–Fe_3O_4 composite was produced by adding different loads of commercial TiO_2 to the synthesis procedure of Fe_3O_4. Next, Ag_3PO_4 was synthesized over the magnetic TiO_2–Fe_3O_4 material by precipitation. The aim of the study was to treat two real wastewaters, namely, effluent from a conventional activated sludge-based WWTP and wastewater from the swimming pool sand filter maintenance system of a hotel, with an Ag_3PO_4-based recoverable photocatalyst.

2. Materials and Methods

2.1. Reagents/Chemicals

Iron (II) chloride ($FeCl_2 \cdot 4H_2O$, 98.0%), iron (III) chloride ($FeCl_3 \cdot 6H_2O$, 97.0%), hydrochloric acid (HCl, 37%), and ammonia solution (NH_3, 25 wt.%), all supplied by Panreac, were used to produce the magnetic material. The titanium dioxide (TiO_2) used in this study was Aeroxide® P25. Silver nitrate ($AgNO_3$, 99.8%), di-sodium hydrogen phosphate ($Na_2HPO_4 \cdot 12H_2O$, 98.5%), and ortho-phosphoric acid (H_3PO_4, 85%), all also supplied by Panreac, were used to synthesize silver phosphate (Ag_3PO_4).

2.2. Analytical Determinations

Scanning electron microscopy (SEM) was performed at a voltage between 8 and 15 kV. A Sigma 300 VP FESEM Zeiss instrument was used, equipped with energy-dispersive X-ray spectroscopy (EDX).

X-ray diffraction (XRD) was performed using a PANalytical Empyrean diffractometer (Cu Kα1, λ = 1.5406 Å). The fractions of the different phases were determined from the relative diffraction peak intensities of the main crystalline planes. Match! 3$^{\circledR}$ software was used to analyze the diffractograms.

The crystallite sizes were calculated from the peak full widths at half maximum (FWHM) using the Scherrer equation [47,48]:

$$\text{Crystallite size (nm)} = K\,\lambda/(\text{FWHM} \cdot \cos\theta) \tag{1}$$

where K is the Scherrer constant (0.9), λ is the wavelength of the radiation (nm), and θ is the diffraction angle of the peak. FWHM values were obtained from Match!3$^{\circledR}$ analysis.

For the X-ray photoelectron spectroscopy (XPS), a PHI VersaProbe II instrument was used. The obtained binding energies were calibrated to the C 1s peak (~284.8 eV). The X-ray source was monochromatic Al Kα (1486.6 eV) at 47.3 W.

The method described in [49] was employed to determine the point of zero charge (pH$_{PZC}$) of the materials. Briefly, several samples were prepared in which 3 mg·mL^{-1} of the material was added to 50 mL of a 0.01 M NaCl solution. The pH of each sample was adjusted to values between 2 and 12 with HCl and/or NaOH, and the samples were left in sealed bottles for 24 h. Next, the pH value of each sample was measured again. The initial pH was plotted against the final pH. The pH$_{PZC}$ was determined from the intersection between the curve and the diagonal line of the plot.

Determination of BET-specific surface areas was carried out from nitrogen adsorption isotherms at −196 °C using a Micromeritics Asap 2020 analyzer (Micromeritics, Norcross, GA, USA).

The hysteresis curves of the magnetic materials were measured at 300 K with a Quantum Design MPMS XL SQUID magnetometer (Quantum Design Iberia, Barcelona, Spain).

A Varian Cary E5 spectrophotometer (200–800 nm) was used for UV–vis diffuse reflectance spectra (DRS) measurements and the bandgap values were determined from the Tauc plot [50].

For COD measurements, USEPA Standard Method 5220 D was followed. Hach$^{\circledR}$ TNT vials were used to determine COD values between 3 and 150 mg·L^{-1}. The digestion of samples, for 2 h at 148 $\pm$ 2 °C, was performed in a SRB200 Hach$^{\circledR}$ reactor Hach Europe, Düsseldorf, Germany).

Standard UNE-EN ISO 9308-3:1999 [51] was followed to determine *E. coli*, and Standard UNE EN ISO 7899-2:2001 [52] was used for *E. faecalis* determination.

The following organic UV filters were determined (from 0.025 μg·L^{-1} to 250 μg·L^{-1}): 4-methylbenzylidene camphor (4-MBC), benzophenone-3 (BP-3), homosalate (HMS), octocrylene (OC), butyl methoxydibenzoylmethane (BMDBM), isoamyl p-methoxycinnamate (IMC), drometrizole trisiloxane (DTS), octisalate (EHS), and methylene bis-benzotriazolyltetramethylbutylphenol (MBP).

For the determination of the abovementioned organic UV filters, the procedure described elsewhere was applied [53]. First, samples were extracted using a solid-phase extraction procedure. Briefly, 700 mL of the samples were adjusted to pH 3 using formic acid and filtered through 0.45 μm. Next, samples were passed through C18 cartridges

and eluted with 5 mL of a methanol: acetonitrile solution (1:1, v/v) to preconcentrate the analytes 140 times.

The samples were then measured in an ACQUITY UHPLC with an MS/MS system (triple quadrupole) equipped with an electrospray ionization (ESI) source. The capillary voltage used was 4 kV, the cone voltage was set to 15 V, and the source temperature was 120 °C. Nitrogen was used for desolvation (450 °C, 500 L·h^{-1}). Argon was used as collision gas. Samples were injected (10 µL) into a BEH C18 column (50 × 2.1 mm, 1.7 µm particle size), with the mobile phase composed of methanol (A) and water with 0.1% (v/v) formic acid (B), at a flow rate of 0.3 mL·min^{-1}. To separate analytes, the mobile phase was applied using the following gradient: 25% A: 75% B for 3 min, then lowered over 2 min to 0% A: 100% B, which was held for 1 more minute. The ratio 25% A: 75% B was next reached in 1 min and held for 1 additional minute before the next injection.

Dissolved iron was determined using the o-phenanthroline method [54] in an Agilent Varian Cary 60 UV–vis spectrophotometer (510 nm). The detection and quantification limits were 0.15 mg·L^{-1} and 0.47 mg·L^{-1}, respectively. The adjusted R^2 was 0.99.

The concentration of silver was determined according to standard UNE-EN ISO 17294 [55], using inductively coupled plasma mass spectrometry (ICP-MS). The detection limit was 2 µg·L^{-1}.

2.3. Synthesis of Materials

The materials synthesized in this study were bare Ag_3PO_4 and the magnetic $Ag_3PO_4@Fe_3O_4$ and $Ag_3PO_4@1\text{-}TiO_2\text{-}Fe_3O_4$. The magnetic supports alone, Fe_3O_4 and $1\text{-}TiO_2\text{-}Fe_3O_4$, were synthesized for comparison purposes.

Ferromagnetite (Fe_3O_4) was synthesized following a modified Massart method [56]. For this purpose, $FeCl_3$ (40 mL, 1 M) and $FeCl_2$ (10 mL, 2 M, prepared in 2 M HCl) were added to an NH_3 solution (500 mL, 0.7 M, pH ≈ 12). The magnetic precipitate formed was washed with deionized water to remove excess NH_3 and then dried at 80 °C for 12 h. The resulting material is Fe_3O_4.

To synthesize the $TiO_2\text{-}Fe_3O_4$ material, TiO_2 (1 g) was added to the NH_3 solution before mixing it with the $FeCl_3$ and $FeCl_2$ solutions. The rest of the procedure was as described above. The resulting material is $1\text{-}TiO_2\text{-}Fe_3O_4$. The TiO_2 used in the synthesis procedure was commercial Evonik P25, which is composed of about 80–85% anatase and 15–20% rutile.

Ag_3PO_4 was supported on the magnetic materials following a method adapted from elsewhere [36]. For this purpose, 104 mg of the magnetic support was dispersed in deionized water and sonicated for 10 min in an Ultrasons-HD Selecta bath (40 kHz). Next, a Na_2HPO_4 (4 mL, 0.15 M) solution at pH 4.12 (regulated with phosphoric acid) was added and the mixture was sonicated for 30 more minutes. Lastly, $AgNO_3$ (12 mL, 0.15 M) was added dropwise, and the mixture was sonicated for 4 h. Next, it was dried at 80 °C, and the solid was washed with deionized water several times to remove impurities. The washed material was dried at 80 °C for 24 h. Lastly, the material was sieved through a 75 µm sieve. The resulting material was named $Ag_3PO_4@Fe_3O_4$ or $Ag_3PO_4@1\text{-}TiO_2\text{-}Fe_3O_4$, depending on the magnetic material employed in the synthesis. To synthesize bare Ag_3PO_4, this same process was applied; however, no magnetic material was added to the mixture.

2.4. Photodegradation Experiments

For the photodegradation experiments, 100 mL (for the WWTP effluent) or 800 mL (for the swimming pool maintenance system wastewater) of wastewater was introduced in a Pyrex glass batch reactor with 1 g·L^{-1} of photocatalyst. This photocatalyst load was chosen as optimal based on preliminary experiments with the WWTP effluent in which the

photocatalyst load varied from 0.5 to 1.5 $g \cdot L^{-1}$. All experiments were conducted at natural pH. The experiments were carried out under solar irradiation. Agitation was maintained by means of strong aeration using a Turbojet M101 aquarium pump (72 $L \cdot h^{-1}$).

For photolysis experiments, the wastewater was left under sunlight without adding photocatalysts. This experiment was performed as a blank experiment to check whether the organic compounds present in the wastewater were susceptible to decomposition under sunlight.

To remove the turbidity of the swimming pool maintenance system wastewater, these samples were filtered through a 1.2 μm filter before the experiments.

The light intensity was measured with a GEO-MS-80-S pyranometer (Eko Instruments, Den Haag, The Netherlands), which is ISO 9060:2018 [57] Class A. The results for these experiments are shown as the percentage of removal of organic matter versus accumulated energy (E_a, $J \cdot L^{-1}$). E_a at different time intervals was calculated following Equation (2) [58],

$$E_a(t) = E(t_0) + \Delta t \cdot \overline{G} \cdot \left(\frac{A}{V} \right) \tag{2}$$

where A is the area exposed to the sunlight, which is the area of the bath reactor, Δt is the reaction time interval, in seconds, $\overline{G}$ is the mean solar irradiation in the time interval, in $W \cdot m^{-2}$, and V is the volume of the treated water, in L.

The reactors were exposed to sunlight once the adsorption–desorption equilibrium was established (i.e., after 30 min in the dark). During irradiation, samples were taken at different time intervals. The catalysts added to the WWTP effluent samples were left to settle in the dark for 5 min and the supernatant was taken for microbiological analysis.

In the recycling experiments, carried out with WWTP effluent samples, the photocatalyst was separated from the solution by centrifugation. The separated photocatalyst was then used in the next degradation experiment without further treatment. For comparison purposes, each cycle of these experiments was continued until the accumulated energy reached 80 $kJ \cdot L^{-1}$. COD removal was registered for each cycle to determine the possible efficiency loss of the photocatalysts.

3. Results and Discussion

### 3.1. Characterisation of the Materials

Representative SEM micrographs of the synthesized materials are shown in Figure 1. All materials presented irregular shapes and heterogeneity in the particle sizes. This was expected because the method chosen to produce them was the chemical precipitation method due to its simplicity and low energy requirements.

EDX elemental mapping analysis revealed that on the surface of the composite materials, iron (Fe), titanium (Ti), and silver (Ag) were distributed along all the surface of the materials, as can be seen in Figure 2 for $Ag_3PO_4@Fe_3O_4$ and $Ag_3PO_4@1\text{-}TiO_2\text{-}Fe_3O_4$. Fe_3O_4 rods were found in different sizes but homogeneously along the image, serving as support for Ag_3PO_4. However, it should be noted that higher concentrations of Ag were found in clusters throughout the surface. These clusters presented variable sizes.

The XRD patterns of all materials are shown in Figure 3. The fractions of each crystalline phase and average crystallite sizes are shown in Table 1. As mentioned above, Match! $3^®$ software and the Crystallography Open Database were used to analyze the diffractograms. The peak with the highest intensity for anatase was found at 2θ equal to 25.3° (corresponding to Miller index 011). For rutile, the main peak was found at 27.4° (110). The position of the main peak for Ag_3PO_4 was 33.4° (201), and that of Fe_3O_4 was 35.7° (311) [59–62].
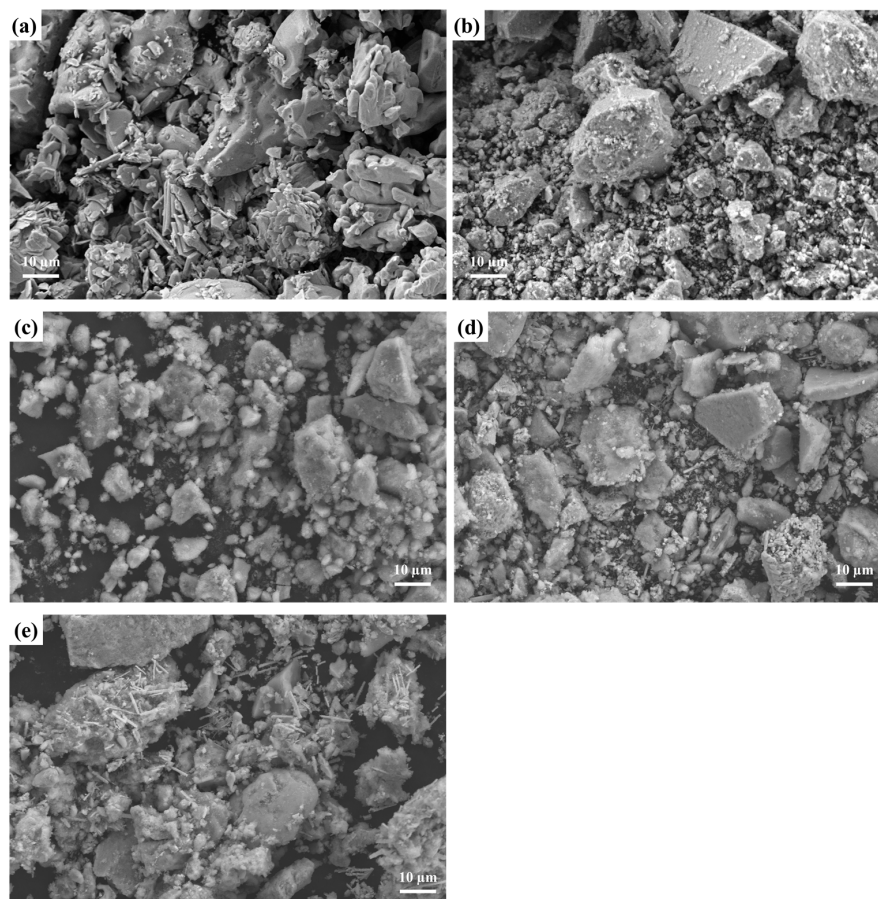
Figure 1. SEM images of (**a**) Ag_3PO_4, (**b**) Fe_3O_4, (**c**) $1\text{-}TiO_2\text{-}Fe_3O_4$, (**d**) $Ag_3PO_4@1\text{-}TiO_2\text{-}Fe_3O_4$, and (**e**) $Ag_3PO_4@ Fe_3O_4$.
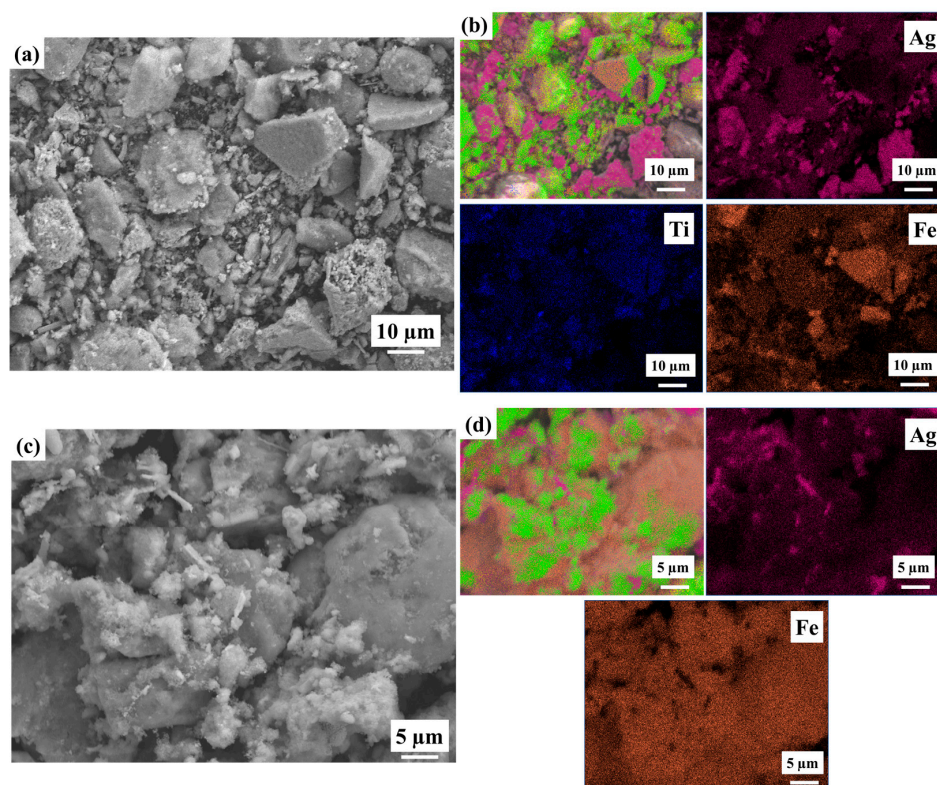
Figure 2. SEM-EDX images of (**a**) $Ag_3PO_4@1\text{-}TiO_2\text{-}Fe_3O_4$, (**b**) EDX map of $Ag_3PO_4@1\text{-}TiO_2\text{-}Fe_3O_4$, (**c**) $Ag_3PO_4@ Fe_3O_4$, and (**d**) EDX map of $Ag_3PO_4@ Fe_3O_4$.
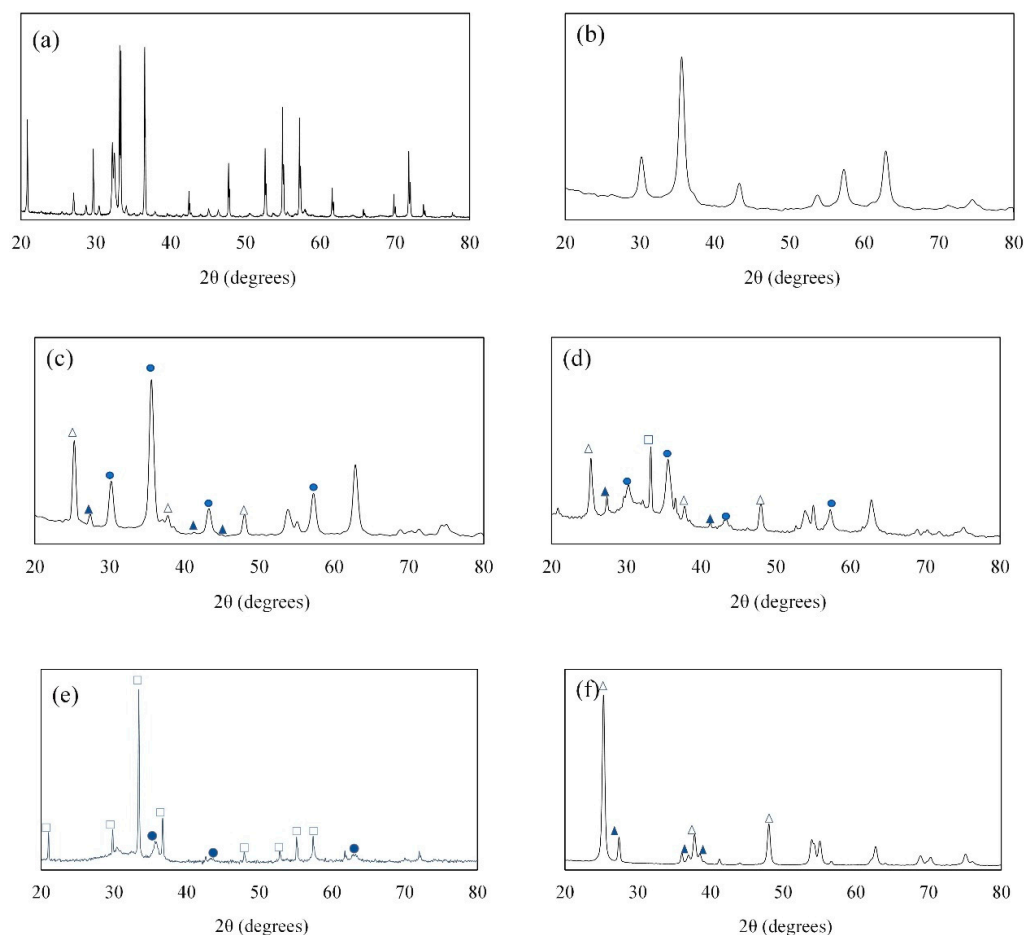
Figure 3. XRD patterns of: (**a**) Ag$_3$PO$_4$, (**b**) Fe$_3$O$_4$, (**c**) 1-TiO$_2$-Fe$_3$O$_4$, (**d**) Ag$_3$PO$_4$@1-TiO$_2$-Fe$_3$O$_4$, (**e**) Ag$_3$PO$_4$@ Fe$_3$O$_4$, and (**f**) TiO$_2$ (Evonik P25). Legend: white square Ag$_3$PO$_4$ (□), dark circle Fe$_3$O$_4$ (●), white triangle TiO$_2$-anatase (△), dark triangle TiO$_2$-rutile (▲).

Table 1. Fraction of the crystalline phases in the composites.

| Material	Ag$_3$PO$_4$	TiO$_2$ (Anatase)	TiO$_2$ (Rutile)	Fe$_3$O$_4$
	%	%	%	%
Ag$_3$PO$_4$	100	-	-	-
Fe$_3$O$_4$	-	-	-	100
1-TiO$_2$-Fe$_3$O$_4$	-	29.6	2.4	68.0
Ag$_3$PO$_4$@1-TiO$_2$-Fe$_3$O$_4$	11.7	24.2	1.7	62.4
Ag$_3$PO$_4$@Fe$_3$O$_4$	61.6	-	-	38.4
TiO$_2$ (Evonik P25)	-	85.5	14.5	-

XRD analysis revealed that, for the 1-TiO$_2$-Fe$_3$O$_4$ material, the presence of the TiO$_2$ crystalline phase anatase was 29.6%. The content of anatase in the Ag$_3$PO$_4$@1-TiO$_2$-Fe$_3$O$_4$ composite was similar (24.2%).

The percentage of Ag$_3$PO$_4$ in Ag$_3$PO$_4$@1-TiO$_2$-Fe$_3$O$_4$ was 11.7%. The Ag$_3$PO$_4$@ Fe$_3$O$_4$ photocatalyst contained 61.6% of Ag$_3$PO$_4$. However, from the SEM-EDX analysis, we observed that the estimated percentage weight of Ag was higher in Ag$_3$PO$_4$@1-TiO$_2$-Fe$_3$O$_4$ than in Ag$_3$PO$_4$@Fe$_3$O$_4$. Thus, although the Ag$_3$PO$_4$@Fe$_3$O$_4$ composite contained a higher ratio of Ag$_3$PO$_4$, the concentration of this photoactive compound was higher on the surface of Ag$_3$PO$_4$@1-TiO$_2$-Fe$_3$O$_4$ than on the surface of Ag$_3$PO$_4$@Fe$_3$O$_4$.

The crystallite sizes were as follows: 52–54 nm for Ag$_3$PO$_4$, 21–22 nm for anatase, 20–22 nm for rutile, and 11–13 nm for Fe$_3$O$_4$. These remained constant for all materials.

XPS analysis was used to further analyze the elemental composition and chemical status of the composites. The three materials were analyzed: Ag_3PO_4, $Ag_3PO_4@Fe_3O_4$, and $Ag_3PO_4@1\text{-}TiO_2\text{-}Fe_3O_4$. Results are shown in Figure 4. Signals of Ag and P were found in all samples. Ag 3d was present in all the materials. For Ag_3PO_4 and $Ag_3PO_4@Fe_3O_4$, this element presented two absorption peaks, at 368.2 eV and 374.1 eV, which correspond to the absorption of Ag 3d5/2 and Ag 3d3/2 orbitals, respectively, with the silver in its ionic form [63]. The peaks were also present in the $Ag_3PO_4@1\text{-}TiO_2\text{-}Fe_3O_4$ composite, although slightly shifted and located at 368.5 and 374.5 eV, respectively. For phosphorus, we found only one P 2p absorption peak at 133.6 eV for all three materials. This corresponds to the phosphate ion in Ag_3PO_4 [64].
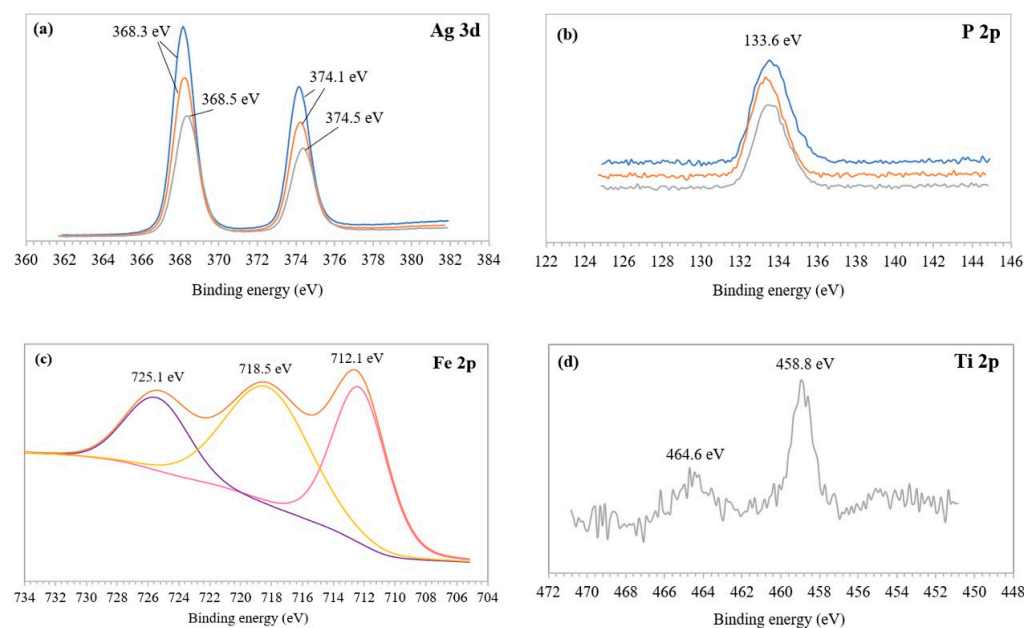
Figure 4. XPS spectra of Ag_3PO_4 (blue), $Ag_3PO_4@Fe_3O_4$ (orange), and $Ag_3PO_4@1\text{-}TiO_2\text{-}Fe_3O_4$ (grey). (**a**) Ag 3d, (**b**) P 2p, (**c**) Fe 2p, and (**d**) Ti 2p.

Fe 2p was determined in the magnetic materials. The deconvoluted spectrum via the Voigt curve fitting function of Fe 2p revealed the following peaks, which are characteristic of Fe_3O_4: Fe 2p3/2 at 712.1 eV and Fe 2p1/2 at 725.1 eV [65].

Lastly, the material containing TiO_2, namely, $Ag_3PO_4@1\text{-}TiO_2\text{-}Fe_3O_4$, presented two Ti 2p absorption peaks (Ti 2p3/2 at 458.8 eV and Ti 2p1/2 at 464.6 eV), which correspond to the Ti^{4+} in TiO_2 [66].

The atomic composition obtained from the XPS studies revealed that the content of silver atoms was 14.91% in $Ag_3PO_4@Fe_3O_4$ and 13.38% in $Ag_3PO_4@1\text{-}TiO_2\text{-}Fe_3O_4$. The atomic content of Ti in this last material was 0.52%.

UV–vis absorption spectra of the studied photocatalysts are included in Figure 5.

From DRS data we observe that, as known, UV illumination ($\lambda < 400$ nm) is required for TiO_2 sensitization. In contrast, visible light up to 530 nm can be used with Ag_3PO_4 and the magnetic composites.

The calculated bandgap (Eg) values of the different materials are shown in Table 2.

We observed that, as expected, TiO_2 had the widest bandgap (3.20 eV). The bandgap of Ag_3PO_4 was 2.36 eV, which agrees with values reported by other authors [16,67]. The bandgap of Fe_3O_4 was the lowest (1.87 eV). This value is similar to that reported by another author for the synthesis of Fe_3O_4 at pH 10 and at room temperature (1.76 eV at 25 °C) [68].
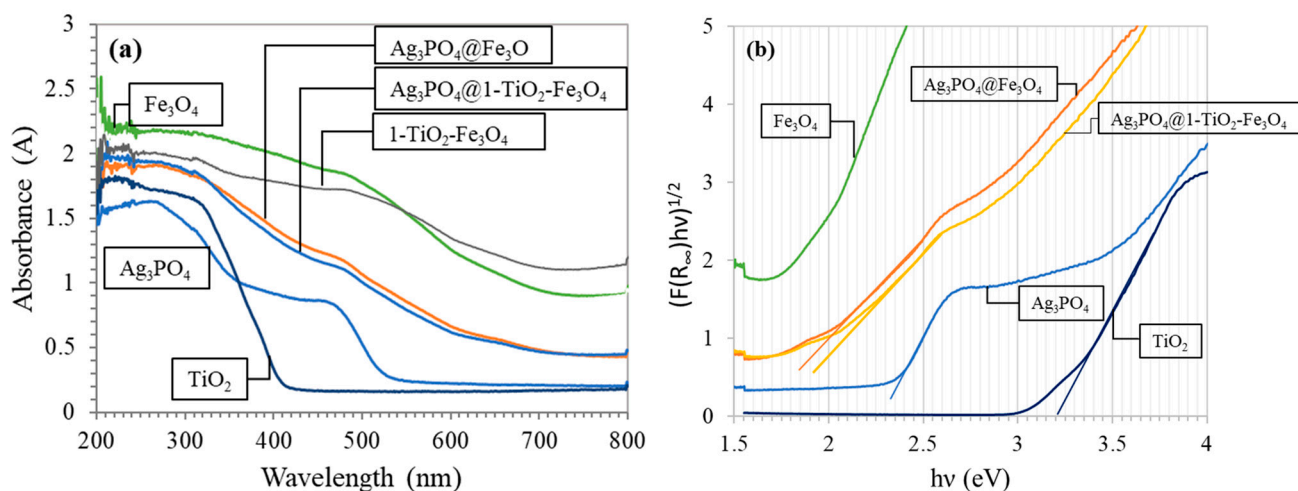
Figure 5. (**a**) UV–vis DRS of the Ag_3PO_4-based photocatalysts and the magnetic supports employed in the study. For comparison purposes, the DRS of TiO_2 (Evonik P25) is also shown. (**b**) Bandgap energy (E_g) determinations from the Tauc plot.

Table 2. Bandgap (E_g), pH_{PZC}, and specific surface area values of the different studied materials.

Material	E_g (eV)	pH_{PZC}	Specific Surface Area ($m^2 \cdot g^{-1}$)
Ag_3PO_4	2.36	5.1	0.80
Fe_3O_4	1.87	7.1	133.99
$Ag_3PO_4@Fe_3O_4$	1.90	7.0	9.82
$Ag_3PO_4@1\text{-}TiO_2\text{-}Fe_3O_4$	2.20	6.5	8.03
TiO_2	3.20	-	52

The estimated pH_{PZC} values were: 5.1 for Ag_3PO_4, 7.1 for Fe_3O_4, 7.0 for $1\text{-}TiO_2\text{-}Fe_3O_4$, 7.0 for $Ag_3PO_4@Fe_3O_4$, and 6.8 for $Ag_3PO_4@1\text{-}TiO_2\text{-}Fe_3O_4$. The pH_{PZC} determined for Ag_3PO_4 agrees with that reported in the literature (pH_{PZC} 4.8) [69]. Likewise, the pH_{PZC} reported by other authors for Fe_3O_4 is between 6.8 and 7.2 [70–72], which is in line with the results we found in this study.

Thus, as reported by other authors [36], Fe_3O_4 particles are expected to be charged positively at pH values below 7.1 (pH_{PZC}), and, for this reason, the addition of phosphate ions at pH 4.12 during the $Ag_3PO_4@Fe_3O_4$ synthesis favors the electrostatic interaction of the negative phosphate groups with the positively charged magnetic particles. The same is applicable to $1\text{-}TiO_2\text{-}Fe_3O_4$, which has a pH_{PZC} of 7.0.

Regarding the specific surface area, we observe from the data shown in Table 2 that the synthesized Ag_3PO_4 presents only 0.80 $m^2 \cdot g^{-1}$. In this sense, several authors have also reported low specific surface areas, between 2.28 and 2.80 $m^2 \cdot g^{-1}$, for Ag_3PO_4 synthesized through the precipitation method, as was carried out in this work [73–76].

We can see from Table 2 that the specific surface area is over 10 times higher for $Ag_3PO_4@Fe_3O_4$ and $Ag_3PO_4@1\text{-}TiO_2\text{-}Fe_3O_4$. That is, the specific surface area of the magnetic composites is higher than that of bare Ag_3PO_4.

The magnetic properties were determined for the following materials: Fe_3O_4, $1\text{-}TiO_2\text{-}Fe_3O_4$, $Ag_3PO_4@Fe_3O_4$, and $Ag_3PO_4@1\text{-}TiO_2\text{-}Fe_3O_4$. The magnetization curves were almost identical for Fe_3O_4 and $1\text{-}TiO_2\text{-}Fe_3O_4$, as well as for $Ag_3PO_4@Fe_3O_4$ and $Ag_3PO_4@1\text{-}TiO_2\text{-}Fe_3O_4$. The magnetization curves of $1\text{-}TiO_2\text{-}Fe_3O_4$ and $Ag_3PO_4@1\text{-}TiO_2\text{-}Fe_3O_4$ are shown in Figure 6a.
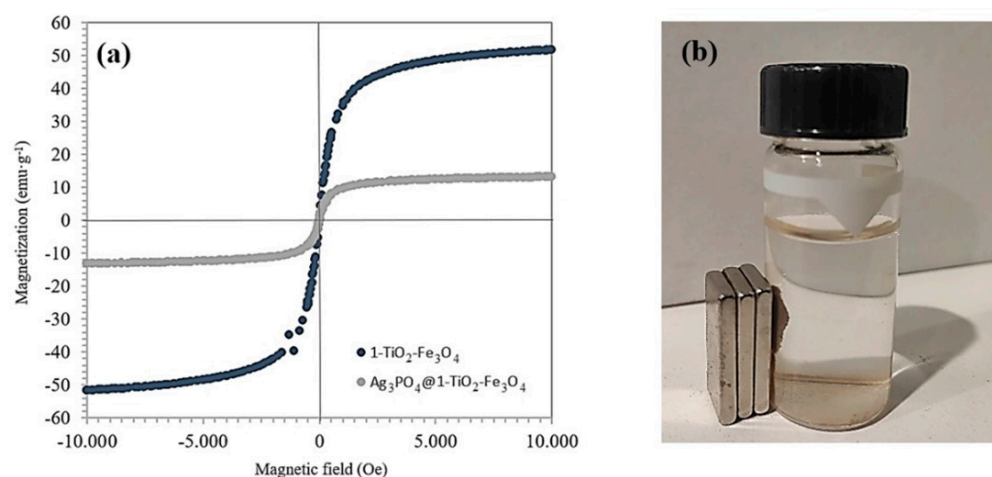
Figure 6. (**a**) Magnetic hysteresis loops of $1\text{-TiO}_2\text{-Fe}_3O_4$ and $Ag_3PO_4@1\text{-TiO}_2\text{-Fe}_3O_4$. (**b**) $Ag_3PO_4@1\text{-}TiO_2\text{-Fe}_3O_4$ separated from water using an external magnet.

The saturation magnetization was 51.6 emu·g^{-1} for $1\text{-TiO}_2\text{-Fe}_3O_4$ and 13.2 emu·g^{-1} for $Ag_3PO_4@1\text{-TiO}_2\text{-Fe}_3O_4$. The decrease in the magnetization observed for the $Ag_3PO_4@1\text{-}TiO_2\text{-Fe}_3O_4$ composite can be attributed to the presence of the non-magnetic Ag_3PO_4. Nonetheless, the composite material presents enough magnetization to be recovered with a magnet in a few seconds. Figure 6b shows a picture of the $Ag_3PO_4@1\text{-TiO}_2\text{-Fe}_3O_4$ material collected with an external magnet.

3.2. Photocatalytic Performance

The photocatalytic materials were tested during the treatment of two different wastewaters, namely, wastewater from the maintenance system of a swimming pool and from a WWTP secondary effluent. The main parameters of both wastewater samples are shown in Table 3.

Table 3. Characterization of the wastewater samples collected from the hotel swimming pool maintenance system and from the WWTP secondary effluent.

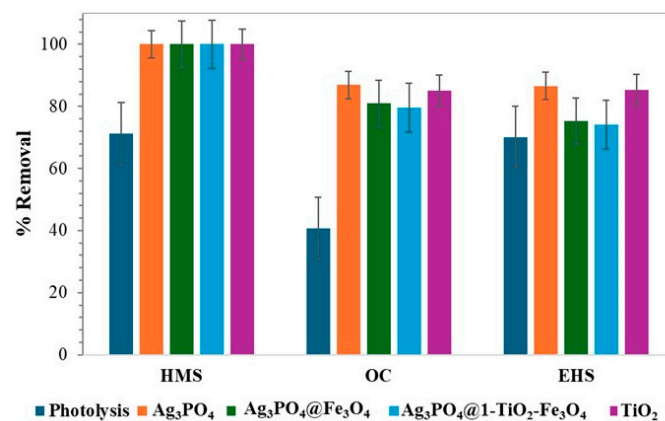| Parameter	Swimming Pool Maintenance System Wastewater	WWTP Secondary Effluent
pH	6.39	6.60
Turbidity (NTU)	31	11.5
COD (mg·L^{-1})	<5	110
Free chlorine (mg·L^{-1})	<0.3	<0.3
E. coli (UFC/100 mL)	<1	-
E. faecalis (UFC/100 mL)	<1	26×10^3

The wastewater from the maintenance system of the swimming pool was filtered to remove turbidity and prevent scattering effects during the photocatalytic process. The wastewater from the WWTP was used as received in the photocatalytic experiments.

3.2.1. Swimming Pool Maintenance System Wastewater

Considering that this wastewater was free of bacteria (see Table 3), the removal of the organic UV filters present in the sample was followed to evaluate the efficiency of the different photocatalysts. Only three organic UV filters (HMS, OC, and EHS) were detected in the wastewater sample from the sand filter maintenance system of the swimming pool, namely, 0.054 ± 0.009 ppb HMS, 1.743 ± 0.012 ppb OC, and 0.137 ± 0.005 ppb EHS. Of

these, OC is included in the EU watch list of priority substances hazardous to the aquatic environment, as indicated previously.

The adsorption of the contaminants on the photocatalysts was negligible. The photocatalytic experiments continued until the accumulated irradiation reached 40 kJ·L^{-1}. Results are shown in Figure 7. It can be observed that 70% of the HMS and EHS was removed through photolysis. OC was less susceptible to photolysis but 40% was removed with exposure to sunlight.

Figure 7. Removal of organic UV filters from the swimming pool maintenance system wastewater. Experimental conditions: 1 g·L^{-1} photocatalyst, natural pH, 40 kJ·L^{-1} accumulated irradiation.

As for the photocatalytic processes, HMS was completely removed from the wastewater sample with all the photocatalysts studied. However, for OC and EHS, bare Ag_3PO_4 and bare TiO_2 presented the highest removal rates. When Ag_3PO_4 was used, 86.91% OC was removed, and 85.05% when TiO_2 was employed. The removal of EHS was 86.56% with Ag_3PO_4 and 85.35% with TiO_2.

Under sunlight, materials with lower bandgap values, such as Ag_3PO_4 (2.36 eV), when compared with TiO_2 (3.2 eV), are expected to present higher photoactivity. However, this also depends on the surface area of the materials, which is available for the adsorption of contaminants and to produce reactive species. In this sense, the specific surface area of Ag_3PO_4 is much lower than that of TiO_2 (see Table 2). Considering that the direct adsorption of contaminants was negligible in this process, it must be considered that Ag_3PO_4 is slightly soluble in water, and it is known that silver ions are reduced to silver atoms (Ag^0) by the photogenerated electrons [16]. This reduces the efficiency of Ag_3PO_4 by increasing the time of exposure to sunlight.

In the swimming pool maintenance system wastewater, the concentration of the contaminants followed along the photocatalytic reactions was low (in the order of µg·L^{-1} or ppb). As mentioned above, both Ag_3PO_4 and TiO_2 presented similar photodegradation results for the removal of UV filters from the wastewater. Thus, we can affirm that, at low contaminant concentrations, both photocatalysts, Ag_3PO_4 and TiO_2, present equal photoactivity under sunlight.

It should be highlighted that, to the best of our knowledge, no previous studies have been conducted on the degradation of these particular UV filters with photocatalysts.

When the magnetic photocatalysts were employed, about 80% OC and 75% EHS were removed. In this case, both materials exhibited very similar efficiencies. The lower removal achieved with the magnetic materials compared to the bare photocatalysts is due to the lower presence of the photoactive materials per mass unit of material. Additionally, it has been reported that ferromagnetite can act as a charge recombination center to the detriment of the photocatalytic process [77]. However, the removal of the organic UV filters was still

high when the magnetic materials were used, and these enabled an easier separation of the photocatalyst from the treated water.

Lastly, it must be noted that the magnetic supports alone, namely, Fe_3O_4 and $1\text{-}TiO_2$-Fe_3O_4, presented negligible photodegradation.

3.2.2. WWTP Secondary Effluent

The photocatalytic activity of the materials was also screened using wastewater from the effluent of the secondary stage of a conventional activated sludge WWTP. On this occasion, the concentration of *E. faecalis* and COD were followed. The experiments were performed using 1 g·L^{-1} of the material, at natural pH, with a 30-min adsorption–desorption equilibrium stage and, next, under sunlight until the accumulated energy reached 80 kJ·L^{-1}. At our location, this accumulated energy was reached in about one hour. It should be noted that *E. faecalis* was completely removed in all the experiments after the illumination stage.

For comparison purposes, experiments were also performed with the magnetic supports alone, in the absence of Ag_3PO_4. We observed that adsorption was negligible for all materials. Fe_3O_4 alone did not produce photodegradation, and Fe_3O_4-$1\text{-}TiO_2$ did show some photoactivity, although the process was very slow, and only 14% COD was removed. Additionally, photolysis experiments were also carried out, with its effect on COD removal having been found to be negligible. Photolysis did, however, remove 100% of the *E. faecalis*, as expected.

The COD removal followed a pseudo-first order reaction kinetic and the reaction rate constants were determined from the slope of the plot $\ln[C/C0]$ vs. reaction time. The apparent reaction rate constants for the COD removal of the WWTP secondary effluent using the photocatalysts studied in this work are shown in Table 4.

Table 4. Apparent reaction rate constant, k, and COD removal for the treatment of a WWTP secondary effluent using the materials studied in this work. Experimental conditions: 1 g·L^{-1} catalyst, natural pH, 80 kJ·L^{-1} accumulated irradiation. *E. faecalis* removal is shown for the adsorption–desorption equilibrium stage (without illumination).

Material	k, min^{-1}	% COD Removal	% *E. faecalis* Removal
Ag_3PO_4	0.0159	62.49%	100%
TiO_2	0.0174	65.82%	7.69%
Ag_3PO_4@ Fe_3O_4	0.0084	39.01%	61.54%
Ag_3PO_4@ Fe_3O_4-1-TiO_2	0.0162	64.67%	65.38%

Among the magnetic Ag_3PO_4 composites, we found that Ag_3PO_4@Fe_3O_4 yielded slower COD removal under sunlight than bare Ag_3PO_4. This suggests that Fe_3O_4 only worked as a support in the composite.

On the other hand, the COD removal with the Ag_3PO_4@1-TiO_2-Fe_3O_4 composite was slightly faster than with bare Ag_3PO_4. This can be attributed to two factors. Firstly, in the magnetic composite, both Ag_3PO_4 and TiO_2 are acting as photocatalysts, thus enhancing the photodegradation process. Secondly, other authors have found that the combination of Ag_3PO_4 and TiO_2 can reduce the electron-hole recombination and, thus, these composites yield higher efficiencies than Ag_3PO_4 alone [78–81]. Furthermore, it has been reported that the production of hydroxyl radicals is higher in an Ag_3PO_4-TiO_2-Fe_3O_4 composite than in bare Ag_3PO_4 [40].

It should be noted that COD removal was very similar for Ag_3PO_4, the commercial TiO_2, and Ag_3PO_4@1-TiO_2-Fe_3O_4, although the apparent degradation rate constant was slightly higher for TiO_2. This can be attributed to the higher surface area of this material compared to the others (see Table 2), and to the fact that Ag_3PO_4 suffers from photocorrosion [16] when exposed to illumination, and thus loses efficiency, as detailed in Section 3.3.

However, only Ag_3PO_4 achieved 100% *E. faecalis* under dark conditions, in the absence of sunlight. This was expected due to the antibacterial properties of silver [82]. The magnetic materials that contained Ag_3PO_4 also removed over 60% *E. faecalis* in the dark stage of the experiments, as depicted in Table 4.

3.3. Reuse of the Magnetic Photocatalysts

The results of the recyclability studies of the magnetic $Ag_3PO_4@Fe_3O_4$ and $Ag_3PO_4@1$-TiO_2-Fe_3O_4 catalysts are shown in Figure 8. We observed that the efficiency of both catalysts decreased with increasing reuse; however, this effect was much sharper for the $Ag_3PO_4@Fe_3O_4$ material.
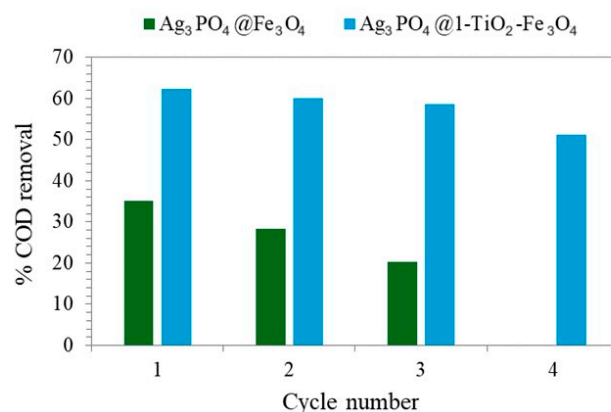
Figure 8. Recyclability studies of the photocatalysts $Ag_3PO_4@Fe_3O_4$ and $Ag_3PO_4@1$-TiO_2-Fe_3O_4. The data shown correspond to the removal of COD from a WWTP secondary effluent with $1\ g \cdot L^{-1}$ photocatalyst after the illumination energy reached $80\ kJ \cdot L^{-1}$.

In this sense, the removal of COD was still about 60% after three reuses with the $Ag_3PO_4@1$-TiO_2-Fe_3O_4 photocatalyst, and the loss in efficiency was observed after the fourth reuse. It should be noted that, in this study, the materials were reused without any treatment.

The loss in efficiency of the photocatalysts with increasing reuse cycles is usually attributed to the reduction of Ag^+ to Ag^0 due to the photocorrosion of Ag_3PO_4. In this sense, it should be noted that the CB edge of Ag_3PO_4 is more positive than E_0 (O_2,aq/$O_2 \cdot^-$) (-0.18 eV vs. NHE) and E_0 (O_2,g/$O_2 \cdot^-$) (-0.33 eV vs. NHE) [83]. For this reason, $O^{2 \cdot -}$ would not be produced from the direct reduction of oxygen when this photocatalyst is used. Thus, the electrons from the CB of Ag_3PO_4 react with Ag^+ ions, which are present due to the slight dissolution of Ag_3PO_4 in water, to form Ag^0 (E0 (Ag^+/Ag^0) is +0.80 V vs. NHE) [84]. This can be seen along the photocatalytic processes with bare Ag_3PO_4 because the material changes from yellow to black.

It is known that Ag-based TiO_2 materials present enhanced photoactivity, mainly because silver can trap the electrons from the conduction band of TiO_2, preventing electron-hole recombination [85]. For this reason, the photocorrosion of Ag_3PO_4 in $Ag_3PO_4@1$-TiO_2-Fe_3O_4 could lead to an enhanced charge separation which may favor the photocatalytic process.

Other authors deduced from XPS analysis that the dissolution of Ag_3PO_4 is greater for bare Ag_3PO_4 than for a Ag_3PO_4-TiO_2-Fe_3O_4 composite [40]. This could explain the better reusability of Ag_3PO_4 composites versus bare Ag_3PO_4.

We performed XRD analysis of both $Ag_3PO_4@1$-TiO_2-Fe_3O_4 and $Ag_3PO_4@Fe_3O_4$ composites after five reuses. XRD analysis of the $Ag_3PO_4@1$-TiO_2-Fe_3O_4 catalyst used (Figure 9) revealed that 15.9% of the Ag_3PO_4 found in the original material was converted to Ag^0. The Ag^0 proportion formed in the $Ag_3PO_4@Fe_3O_4$ composite was similar. Thus, in

this study, the photocorrosion of Ag_3PO_4 was not inhibited in the composite that contained TiO_2.
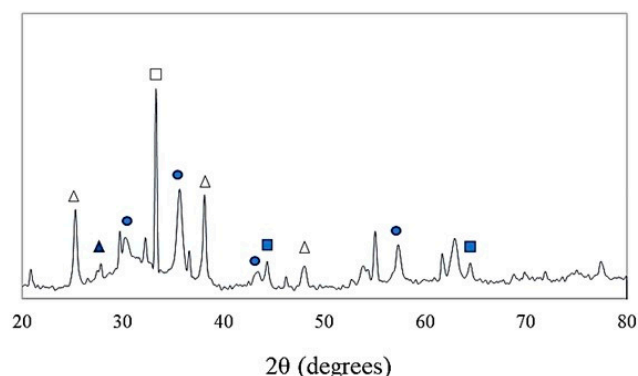
Figure 9. XRD pattern of Ag_3PO_4@1-TiO_2-Fe_3O_4 after five reuses. Legend: white square Ag_3PO_4 (□), dark square Ag^0 (■), dark circle Fe_3O_4 (●), white triangle TiO_2-anatase (△), dark triangle TiO_2-rutile (▲).

Therefore, the best performance of the Ag_3PO_4@1-TiO_2-Fe_3O_4 composite versus Ag_3PO_4@Fe_3O_4 in the recyclability studies may be attributed to the presence of two photocatalysts, Ag_3PO_4 and TiO_2, and the additional presence of Ag^0 in the Ag_3PO_4@1-TiO_2-Fe_3O_4 material. As explained above, Ag^0 formed on the surface of Ag_3PO_4 may act as an electron acceptor and further enhance charge separation.

Lastly, it is known that one of the major issues in the use of silver-based catalysts is that they can exhibit high toxicity [86]. In this sense, it has been reported that free silver ions released from the catalysts play a considerable role in the toxicity of these materials [87].

For this reason, we determined the concentration of silver in water after the photocatalytic processes at pH 9 when the following photocatalysts were used: bare Ag_3PO_4, Ag_3PO_4@Fe_3O_4, and Ag_3PO_4@1-TiO_2-Fe_3O_4. We found that the concentration of silver was high (83.41 $mg\cdot L^{-1}$) when bare Ag_3PO_4 was used. However, for the Ag_3PO_4@Fe_3O_4 and Ag_3PO_4@1-TiO_2-Fe_3O_4 composites, the release of silver was 240 and 478 $\mu g\cdot L^{-1}$, respectively. This shows that the presence of both Fe_3O_4 and 1-TiO_2-Fe_3O_4 in the materials inhibits the release of silver into the water media. The release of silver reported in this study is much lower than that reported by other authors, which can reach up to 0.12 $g\cdot L^{-1}$ [40].

However, further studies are needed to further reduce the dissolution lixiviation of silver from the photocatalysts. As a reference, to date, the World Health Organization (WHO) reports that 100 $\mu g\cdot L^{-1}$ silver is the health-based acceptable reference value in potable water [88].

Regarding the dissolution lixiviation of iron, it was lower than 0.47 $mg\cdot L^{-1}$ for the magnetic composites when used at pH > 6. It should be noted that the concentration of iron in water is frequently limited by legislation. In the Canary Islands (Spain), this limit is 10 $mg\cdot L^{-1}$ for wastewater disposal, according to Decree 2/2019. Similarly, no more than 2 $mg\cdot L^{-1}$ iron is accepted for water reuse, according to the national Royal Decree 1620/2007.

4. Conclusions

A novel magnetically recoverable Ag_3PO_4-TiO_2-Fe_3O_4 photocatalyst was synthesized and studied in this work for the treatment of two different real wastewaters. To the best of our knowledge, no similar studies have previously been published in the literature. The wastewater from the sand filter maintenance system of the swimming pool of a hotel in the south of Gran Canaria (Spain) presented three UV filters, namely, HMS, EHS, and OC. This last compound was included in 2022 in the EU watch list of priority substances hazardous

to the aquatic environment. Over 75% of all sunscreen molecules were removed with the photocatalysts studied in this work, using 40 kJ·L^{-1} of sunlight. The treatment of a WWTP effluent indicated that only the materials that contained Ag$_3$PO$_4$ presented a bactericidal effect under dark conditions. COD removal (over 60%) was very similar for Ag$_3$PO$_4$, the commercial TiO$_2$, and Ag$_3$PO$_4$@1-TiO$_2$-Fe$_3$O$_4$ for accumulated energy of 80 kJ·L^{-1}. However, the dissolution of silver, which is known to be highly toxic, was greatly reduced for the Ag$_3$PO$_4$-based magnetic materials compared to bare Ag$_3$PO$_4$. The dissolution of silver was over 80 mg·L^{-1} for bare Ag$_3$PO$_4$ and was reduced to less than 500 μg·L^{-1} for the magnetic Ag$_3$PO$_4$-based composites. The magnetic materials were recovered easily with a magnet. The saturation magnetization was 51.6 emu·g^{-1} for 1-TiO$_2$-Fe$_3$O$_4$ and 13.2 emu·g^{-1} for Ag$_3$PO$_4$@1-TiO$_2$-Fe$_3$O$_4$. Finally, Ag$_3$PO$_4$@1-TiO$_2$-Fe$_3$O$_4$ could be reused four times with an efficiency loss of 15%. It should be noted that the materials were not washed or treated between reuses. Future works should focus on improving the materials in terms of achieving lower silver dissolution and better stability for their reuse.

Author Contributions: D.E.S.: Conceptualization; Data curation; Formal analysis; Investigation; Methodology; Resources; Software; Validation; Visualization; Writing—original draft; Writing—review and editing. J.V.R.: Conceptualization; Data curation; Investigation; Methodology; Resources; Validation; Visualization; Writing—review and editing. J.J.S.A.: Formal analysis; Funding acquisition; Project administration; Resources; Methodology; Technical research meetings; Supervision; Validation. All authors have read and agreed to the published version of the manuscript.

Data Availability Statement: The original contributions presented in this study are included in the article. Further inquiries can be directed to the corresponding author. The raw data supporting the conclusions of this article will be made available by the authors on request.

Conflicts of Interest: The authors declare no conflicts of interest. The funders had no role in the design of the study; in the collection, analyses, or interpretation of data; in the writing of the manuscript; or in the decision to publish the results.

References

1. Jiang, T.; Wu, W.; Ma, M.; Hu, Y.; Li, R. Occurrence and Distribution of Emerging Contaminants in Wastewater Treatment Plants: A Globally Review over the Past Two Decades. *Sci. Total Environ.* **2024**, *951*, 175664. [CrossRef] [PubMed]
2. Council of the European Community. *Council Directive 91/271/EEC of 21 May 1991 Concerning Urban Waste-Water Treatment*; L135; EU: Brussels, Belgium, 1991; pp. 0040–0052.
3. Pereira, L.C.; de Souza, A.O.; Bernardes, M.F.F.; Pazin, M.; Tasso, M.J.; Pereira, P.H.; Dorta, D.J. A Perspective on the Potential Risks of Emerging Contaminants to Human and Environmental Health. *Environ. Sci. Pollut. Res.* **2015**, *22*, 13800–13823. [CrossRef]
4. Lozano, C.; Matallana-Surget, S.; Givens, J.; Nouet, S.; Arbuckle, L.; Lambert, Z.; Lebaron, P. Toxicity of UV Filters on Marine Bacteria: Combined Effects with Damaging Solar Radiation. *Sci. Total Environ.* **2020**, *722*, 137803. [CrossRef]
5. Lee, S.; Ka, Y.; Lee, B.; Lee, I.; Seo, Y.E.; Shin, H.; Kho, Y.; Ji, K. Single and Mixture Toxicity Evaluation of Avobenzone and Homosalate to Male Zebrafish and H295R Cells. *Chemosphere* **2023**, *343*, 140271. [CrossRef]
6. Taheran, M.; Naghdi, M.; Brar, S.K.; Verma, M.; Surampalli, R.Y. Emerging Contaminants: Here Today, There Tomorrow! *Environ. Nanotechnol. Monit. Manag.* **2018**, *10*, 122–126. [CrossRef]
7. Kagle, J.; Porter, A.W.; Murdoch, R.W.; Rivera-Cancel, G.; Hay, A.G. Chapter 3 Biodegradation of Pharmaceutical and Personal Care Products. *Adv. Appl. Microbiol.* **2009**, *67*, 65–108. [CrossRef]
8. The European Parliament and the Council of the European Union. *Directive 2013/39/EU of the European Parliament and of the Council of 12 August 2013 Amending Directives 2000/60/EC and 2008/105/EC as Regards Priority Substances in the Field of Water Policy*; European Union: Brussels, Belgium, 2013; pp. 1–17.

9. European Commission. *Decision (EU) 2022/1307 of 22 July 2022 Establishing a Watch List of Substances for Union-Wide Monitoring in the Field of Water Policy Pursuant to Directive 2008/105/EC of the European Parliament and of the Council*; European Union: Brussels, Belgium, 2022; pp. 117–121.

10. Torres-Padrón, M.E.; Montesdeoca-Esponda, S.; Santana-Viera, S.; Guedes-Alonso, R.; Herrera-Melián, J.A.; Sosa-Ferrera, Z.; Santana-Rodríguez, J.J. An Update of the Occurrence of Organic Contaminants of Emerging Concern in the Canary Islands (Spain). *Water* **2020**, *12*, 2548. [CrossRef]

11. Liu, Y.; Ohko, Y.; Zhang, R.; Yang, Y.; Zhang, Z. Degradation of Malachite Green on Pd/WO_3 Photocatalysts under Simulated Solar Light. *J. Hazard. Mater.* **2010**, *184*, 386–391. [CrossRef] [PubMed]

12. Malato-Rodríguez, S. Solar Detoxification and Disinfection. In *Encyclopedia of Energy*; Elsevier: Amsterdam, The Netherlands, 2004; pp. 587–596. [CrossRef]

13. Zhuang, H.; Chen, X.; Xia, J.; Lu, K.; Huang, W.; Liu, X.; Yu, C.; Yang, K. State-of-the-Art Progress in Ag_3PO_4-Based Photocatalysts: Rational Design, Regulation and Perspective. *Appl. Mater. Today* **2023**, *31*, 101742. [CrossRef]

14. Yi, Z.; Ye, J.; Kikugawa, N.; Kako, T.; Ouyang, S.; Stuart-Williams, H.; Yang, H.; Cao, J.; Luo, W.; Li, Z.; et al. An Orthophosphate Semiconductor with Photooxidation Properties under Visible-Light Irradiation. *Nat. Mater.* **2010**, *9*, 559–564. [CrossRef]

15. Amirulsyafiee, A.; Khan, M.M.; Harunsani, M.H. Ag_3PO_4 and Ag_3PO_4–Based Visible Light Active Photocatalysts: Recent Progress, Synthesis, and Photocatalytic Applications. *Catal. Commun.* **2022**, *172*, 106556. [CrossRef]

16. Yu, C.; Chen, X.; Li, N.; Zhang, Y.; Li, S.; Chen, J.; Yao, L.; Lin, K.; Lai, Y.; Deng, X. Ag_3PO_4-Based Photocatalysts and Their Application in Organic-Polluted Wastewater Treatment. *Environ. Sci. Pollut. Res.* **2022**, *29*, 18423–18439. [CrossRef]

17. Zhang, X.; Yi, G.; Li, P.; Zheng, X.; Shen, X.; Ning, K.; Chen, L.; Zhang, C.; Zhang, Y.; Sun, Q. Construction of Nitrogen Vacant $G-C_3N_4$ Nanosheet Supported Ag_3PO_4 Nanoparticle Z-Scheme Photocatalyst for Improved Visible-Light Photocatalytic Activity. *Environ. Sci. Pollut. Res.* **2022**, *29*, 23094–23103. [CrossRef]

18. Ding, N.; Fei, Q.; Xiao, D.; Zhang, H.; Yin, H.; Yuan, C.; Lv, H.; Gao, P.; Zhang, Y.; Wang, R. Highly Efficient and Recyclable Z-Scheme Heterojunction of $Ag_3PO_4/g-C_3N_4$ Floating Foam for Photocatalytic Inactivation of Harmful Algae under Visible Light. *Chemosphere* **2023**, *317*, 137773. [CrossRef]

19. Zhang, M.; Du, H.; Ji, J.; Li, F.; Lin, Y.C.; Qin, C.; Zhang, Z.; Shen, Y. Highly Efficient $Ag_3PO_4/g-C_3N_4$ Z-Scheme Photocatalyst for Its Enhanced Photocatalytic Performance in Degradation of Rhodamine B and Phenol. *Molecules* **2021**, *26*, 2062. [CrossRef]

20. Sadeghi Farshi, F.; Behnajady, M.A.; Aberoomand Azar, P.; Safekordi, A.A.; Modirshahla, N. A Mechanistic Study on Photocatalytic Activity of Hydrothermally Synthesized Titanium Dioxide Nanowires Decorated by Silver Phosphate. *Mater. Sci. Semicond. Process* **2022**, *142*, 106501. [CrossRef]

21. Gan, W.; Fu, X.; Guo, J.; Zhang, M.; Yu, H.; Ding, C.; Qi, S.; Cao, X.; Sun, Z. Facile Synthesis of Mesoporous Hierarchical TiO_2 Micro-Flowers Serving as the Scaffolding of 0D Ag_3PO_4 Nanoparticles for the Ultra-Fast Degradation of Organic Pollutants. *J. Alloys Compd.* **2022**, *909*, 164737. [CrossRef]

22. Hou, C.; Li, Y.; Niu, M.; Liu, Y.; Kong, X.; Zhang, M.; Wang, L. Construction of an All-Solid-State Z-Scheme $Ag@Ag_3PO_4/TiO_2$-(F2) Heterostructure with Enhanced Photocatalytic Activity, Photocorrosion Resistance and Mechanism Insight. *J. Alloys Compd.* **2022**, *925*, 166765. [CrossRef]

23. Ma, X.; Li, H.; Wang, Y.; Li, H.; Liu, B.; Yin, S.; Sato, T. Substantial Change in Phenomenon of "Self-Corrosion" on Ag_3PO_4/TiO_2 Compound Photocatalyst. *Appl. Catal. B* **2014**, *158–159*, 314–320. [CrossRef]

24. Li, Y.; Wang, P.; Huang, C.; Yao, W.; Wu, Q.; Xu, Q. Synthesis and Photocatalytic Activity of Ultrafine Ag3PO4 Nanoparticles on Oxygen Vacated TiO_2. *Appl. Catal. B* **2017**, *205*, 489–497. [CrossRef]

25. Moeini, Z.; Hoseini, M.; Dehghani, M.; Samaei, M.; Jafari, S.; Taghavi, M.; Azhdarpoor, A. Synthesize of Heterostructure TiO_2 by Simultaneous Doping of Double Silver and Phosphate to Degradation of Methylene Blue under Visible Light. *Appl. Water Sci.* **2024**, *14*, 39. [CrossRef]

26. Chen, X.; Dai, Y.; Wang, X. Methods and Mechanism for Improvement of Photocatalytic Activity and Stability of Ag_3PO_4: A Review. *J. Alloys Compd.* **2015**, *649*, 910–932. [CrossRef]

27. Chen, F.; Yang, Q.; Li, X.; Zeng, G.; Wang, D.; Niu, C.; Zhao, J.; An, H.; Xie, T.; Deng, Y. Hierarchical Assembly of Graphene-Bridged $Ag_3PO_4/Ag/BiVO_4$ (040) Z-Scheme Photocatalyst: An Efficient, Sustainable and Heterogeneous Catalyst with Enhanced Visible-Light Photoactivity towards Tetracycline Degradation under Visible Light Irradiation. *Appl. Catal. B* **2017**, *200*, 330–342. [CrossRef]

28. Chen, Z.; Li, X.; Xu, Q.; Tao, Z.; Yao, F.; Huang, X.; Wu, Y.; Wang, D.; Jiang, P.; Yang, Q. Three-Dimensional Network Space $Ag_3PO_4/NP-CQDs/RGH$ for Enhanced Organic Pollutant Photodegradation: Synergetic Photocatalysis Activity/Stability and Effect of Real Water Quality Parameters. *Chem. Eng. J.* **2020**, *390*, 124454. [CrossRef]

29. Luo, C.; Lin, Y.; Zhang, Y.; Zhang, S.; Tong, S.; Wu, S.; Yang, C. S-Scheme Heterojunction between MOFs and Ag_3PO_4 Leads to Efficient Photodegradation of Antibiotics in Swine Wastewater. *Sep. Purif. Technol.* **2023**, *320*, 124052. [CrossRef]

30. Sharma, A.; Ming, J.; Liu, N.; Sun, X.; Zhu, Y.; Yano, M.; Chen, G.; Yang, Y. Sustainable and Efficient Reduction of Pollutants by Immobilized PEG-P/Ag/Ag$_2$O/Ag$_3$PO$_4$/TiO$_2$ Photocatalyst for Purification of Saline Wastewater. *Mar. Pollut. Bull.* **2022**, *179*, 113731. [CrossRef]

31. Huang, T.Y.; Chen, Y.J.; Lai, C.Y.; Lin, Y.W. Synthesis, Characterization, Enhanced Sunlight Photocatalytic Properties, and Stability of Ag/Ag$_3$PO$_4$ Nanostructure-Sensitized BiPO$_4$. *RSC Adv.* **2015**, *5*, 43854–43862. [CrossRef]

32. Bekele, T. Synthesis and Characterization of CeO$_2$/Ag$_3$PO$_4$ p-n Heterojunction Photocatalyst: Its Photocatalytic Activity for the Degradation of Alizarin Yellow Dye. *J. Nanomater.* **2023**, *2023*, 7140181. [CrossRef]

33. Zhang, D.; Li, Y.; Chen, X.; Li, C.; Dong, L.; Wang, Z. Wide Spectra-Responsive Polypyrrole-Ag$_3$PO$_4$/BiPO$_4$ Co-Coupled TiO$_2$ Nanotube Arrays for Intensified Photoelectrocatalysis Degradation of PFOA. *Sep. Purif. Technol.* **2022**, *287*, 120521. [CrossRef]

34. Santiago, D.E.; Espino-Estévez, M.R.; González, G.V.; Araña, J.; González-Díaz, O.; Doña-Rodríguez, J.M. Photocatalytic Treatment of Water Containing Imazalil Using an Immobilized TiO$_2$ Photoreactor. *Appl. Catal. A Gen.* **2015**, *498*, 1–9. [CrossRef]

35. Chen, Y.; Jin, X. Preparation of Fe$_3$O$_4$@SiO$_2$@BiO$_{1.8}$·0.04H$_2$O/Ag$_3$PO$_4$ Magnetic Nanocomposite and Its Photocatalytic Performance. *Ceram. Int.* **2019**, *45*, 1283–1292. [CrossRef]

36. Guo, X.; Chen, N.; Feng, C.; Yang, Y.; Zhang, B.; Wang, G.; Zhang, Z. Performance of Magnetically Recoverable Core-Shell Fe$_3$O$_4$@Ag$_3$PO$_4$/AgCl for Photocatalytic Removal of Methylene Blue under Simulated Solar Light. *Catal. Commun.* **2013**, *38*, 26–30. [CrossRef]

37. Jin, H.; Dong, J.; Qu, X. Magnetic Organic Polymer Gel Decorating Ag$_3$PO$_4$ as Z-Scheme Photocatalyst for Water Decontamination. *Colloids Surf. A Physicochem. Eng. Asp.* **2021**, *614*, 126160. [CrossRef]

38. Mousavi, M.; Habibi-Yangjeh, A. Novel Magnetically Separable G-C$_3$N$_4$/Fe$_3$O$_4$/Ag$_3$PO$_4$/Co$_3$O$_4$ Nanocomposites: Visible-Light-Driven Photocatalysts with Highly Enhanced Activity. *Adv. Powder Technol.* **2017**, *28*, 1540–1553. [CrossRef]

39. Shekofteh-Gohari, M.; Habibi-Yangjeh, A. Photosensitization of Fe$_3$O$_4$/ZnO by AgBr and Ag$_3$PO$_4$ to Fabricate Novel Magnetically Recoverable Nanocomposites with Significantly Enhanced Photocatalytic Activity under Visible-Light Irradiation. *Ceram. Int.* **2016**, *42*, 15224–15234. [CrossRef]

40. Xu, J.W.; Gao, Z.D.; Han, K.; Liu, Y.; Song, Y.Y. Synthesis of Magnetically Separable Ag$_3$PO$_4$/TiO$_2$/Fe$_3$O$_4$ heterostructure with Enhanced Photocatalytic Performance under Visible Light for Photoinactivation of Bacteria. *ACS Appl. Mater. Interfaces* **2014**, *6*, 15122–15131. [CrossRef]

41. Wang, C.; Cao, M.; Wang, P.; Ao, Y.; Hou, J.; Qian, J. Preparation of a Magnetic Graphene Oxide-Ag$_3$PO$_4$ Composite Photocatalyst with Enhanced Photocatalytic Activity under Visible Light Irradiation. *J. Taiwan Inst. Chem. Eng.* **2014**, *45*, 1080–1086. [CrossRef]

42. Ji, Z.; Zhao, J.; Shen, X.; Yue, X.; Yuan, A.; Zhou, H.; Yang, J. Construction of Magnetically Separable Ag$_3$PO$_4$/Fe$_3$O$_4$/GO Composites as Recyclable Photocatalysts. *Ceram. Int.* **2015**, *41*, 13509–13515. [CrossRef]

43. Abroshan, E.; Farhadi, S.; Zabardasti, A. Novel Magnetically Separable Ag$_3$PO$_4$/MnFe$_2$O$_4$ Nanocomposite and Its High Photocatalytic Degradation Performance for Organic Dyes under Solar-Light Irradiation. *Sol. Energy Mater. Sol. Cells* **2018**, *178*, 154–163. [CrossRef]

44. Liu, Z.; Feng, H.; Xue, S.; Xie, P.; Li, L.; Hou, X.; Gong, J.; Wei, X.; Huang, J.; Wu, D. The Triple-Component Ag$_3$PO$_4$-CoFe$_2$O$_4$-GO Synthesis and Visible Light Photocatalytic Performance. *Appl. Surf. Sci.* **2018**, *458*, 880–892. [CrossRef]

45. Chen, Y.; Zhu, P.; Duan, M.; Li, J.; Ren, Z.; Wang, P. Fabrication of a Magnetically Separable and Dual Z-Scheme PANI/Ag$_3$PO$_4$/NiFe$_2$O$_4$ Composite with Enhanced Visible-Light Photocatalytic Activity for Organic Pollutant Elimination. *Appl. Surf. Sci.* **2019**, *486*, 198–211. [CrossRef]

46. Mitoraj, D.; Lamdab, U.; Kangwansupamonkon, W.; Pacia, M.; Macyk, W.; Wetchakun, N.; Beranek, R. Revisiting the Problem of Using Methylene Blue as a Model Pollutant in Photocatalysis: The Case of InVO$_4$/BiVO$_4$ Composites. *J. Photochem. Photobiol. A Chem.* **2018**, *366*, 103–110. [CrossRef]

47. Langford, J.I.; Wilson, A.J.C. Scherrer after Sixty Years: A Survey and Some New Results in the Determination of Crystallite Size. *J. Appl. Crystallogr.* **1978**, *11*, 102–113. [CrossRef]

48. Scherrer, P. Bestimmung Der Größe Und Der Inneren Struktur von Kolloidteilchen Mittels Röntgenstrahlen. In Proceedings of the Nachrichten von der Gesellschaft der Wissenschaften zu Göttingen, Mathematisch-Physikalische Klasse; Physikalisches Institut: Göttingen, Germany; 1918; pp. 98–100.

49. Rivera-Utrilla, J.; Bautista-Toledo, I.; Ferro-Garca, M.A.; Moreno-Castilla, C. Activated Carbon Surface Modifications by Adsorption of Bacteria and Their Effect on Aqueous Lead Adsorption. *J. Chem. Technol. Biotechnol.* **2001**, *76*, 1209–1215. [CrossRef]

50. Makuła, P.; Pacia, M.; Macyk, W. How To Correctly Determine the Band Gap Energy of Modified Semiconductor Photocatalysts Based on UV-Vis Spectra. *J. Phys. Chem. Lett.* **2018**, *9*, 6814–6817. [CrossRef]

51. *UNE-EN ISO 9308-3:1999*; Calidad del Agua. Detección y Recuento de *Escherichia coli* y Bacterias Coliformes. Parte 3: Método Mniaturizado (Número Más Probable) para la Detección y Recuento de *E. coli* en Aguas Superficiales y Aguas Residuales. AENOR: Madrid, Spain, 1999.

52. *NE-EN ISO 7899-2:2001*; Calidad del Agua. Detección y Recuento de Enterococos Intestinales. Parte 2: Método de Filtración de Membrana. AENOR: Madrid, Spain, 2001.

53. Cadena-Aizaga, M.I.; Montesdeoca-Esponda, S.; Sosa-Ferrera, Z.; Santana-Rodríguez, J.J. Occurrence and Environmental Hazard of Organic UV Filters in Seawater and Wastewater from Gran Canaria Island (Canary Islands, Spain). *Environ. Pollut.* **2022**, *300*, 118843. [CrossRef]

54. Saywell, L.G.; Cunningham, B.B. Determination of Iron: Colorimetric o-Phenanthroline Method. *Ind. Eng. Chem. Anal. Ed.* **1937**, *9*, 67–69. [CrossRef]

55. *UNE-EN ISO 17294*; Calidad del Agua. Aplicación de la Espectrometría de Masas con Plasma Acoplado Inductivamente (ICP-MS). AENOR: Madrid, Spain, 2017.

56. Massart, R. Preparation of Aqueous Magnetic Liquids in Alkaline and Acidic Media. *IEEE Trans. Magn.* **1981**, *17*, 1247–1248. [CrossRef]

57. *ISO 9060:2018*; Solar Energy — Specification and Classification of Instruments for Measuring Hemispherical Solar and Direct Solar Radiation. ISO (the International Organization for Standardization): Geneva, Switzerland, 2018.

58. Spasiano, D.; Marotta, R.; Malato, S.; Fernandez-Ibañez, P.; Di Somma, I. Solar Photocatalysis: Materials, Reactors, Some Commercial, and Pre-Industrialized Applications. A Comprehensive Approach. *Appl. Catal. B* **2015**, *170–171*, 90–123. [CrossRef]

59. Gražulis, S.; Daš Kevič, A.; Merkys, A.; Chateigner, D.; Lutterotti, L.; Quiró, M.; Serebryanaya, N.R.; Moeck, P.; Downs, R.T.; Le Bail, A. Crystallography Open Database (COD): An Open-Access Collection of Crystal Structures and Platform for World-Wide Collaboration. *Nucleic Acids Res.* **2012**, *40*, 420–427. [CrossRef]

60. Vaitkus, A.; Merkys, A.; Gražulis, S. Validation of the Crystallography Open Database Using the Crystallographic Information Framework. *J. Appl. Crystallogr.* **2021**, *54*, 661–672. [CrossRef]

61. Gražulis, S.; Chateigner, D.; Downs, R.T.; Yokochi, A.F.T.; Quirós, M.; Lutterotti, L.; Manakova, E.; Butkus, J.; Moeck, P.; Le Bail, A. Crystallography Open Database—An Open-Access Collection of Crystal Structures. *J. Appl. Crystallogr.* **2009**, *42*, 726–729. [CrossRef]

62. Downs, R.T.; Hall-Wallace, M. The American Mineralogist Crystal Structure Database. *Am. Mineral.* **2003**, *88*, 247–250.

63. You, M.; Pan, J.; Chi, C.; Wang, B.; Zhao, W.; Song, C.; Zheng, Y.; Li, C. The Visible Light Hydrogen Production of the Z-Scheme Ag_3PO_4/Ag/g-C_3N_4 Nanosheets Composites. *J. Mater. Sci.* **2018**, *53*, 1978–1986. [CrossRef]

64. Amaral, R.; Blois, C.; Lunz, J.; Mello, A.; Jardim, P. Physical and Optical Properties of Ag_3PO_4 Decorated TiO_2 Based Nanostructures. *J. Solid. State Chem.* **2022**, *305*, 122655. [CrossRef]

65. Kohzadi, H.; Soleiman-Beigi, M. XPS and Structural Studies of Fe_3O_4-PTMS-NAS@Cu as a Novel Magnetic Natural Asphalt Base Network and Recoverable Nanocatalyst for the Synthesis of Biaryl Compounds. *Sci. Rep.* **2021**, *11*, 24508. [CrossRef]

66. Devan, R.S.; Thakare, V.P.; Antad, V.V.; Chikate, P.R.; Khare, R.T.; More, M.A.; Dhayal, R.S.; Patil, S.I.; Ma, Y.R.; Schmidt-Mende, L. Nano-Heteroarchitectures of Two-Dimensional MoS_2@ One-Dimensional Brookite TiO_2 Nanorods: Prominent Electron Emitters for Displays. *ACS Omega* **2017**, *2*, 2925–2934. [CrossRef]

67. Liu, J.J.; Fu, X.L.; Chen, S.F.; Zhu, Y.F. Electronic Structure and Optical Properties of Ag_3PO_4 Photocatalyst Calculated by Hybrid Density Functional Method. *Appl. Phys. Lett.* **2011**, *99*, 191903. [CrossRef]

68. Saragi, T.; Depi, B.L.; Butarbutar, S.; Permana, B.; Risdiana. The Impact of Synthesis Temperature on Magnetite Nanoparticles Size Synthesized by Co-Precipitation Method. *J. Phys. Conf. Ser.* **2018**, *1013*, 012190. [CrossRef]

69. Li, S.; Zhang, M.; Qu, Z.; Cui, X.; Liu, Z.; Piao, C.; Li, S.; Wang, J.; Song, Y. Fabrication of Highly Active Z-Scheme Ag/g-C_3N_4-Ag-Ag_3PO_4 (1 1 0) Photocatalyst Photocatalyst for Visible Light Photocatalytic Degradation of Levofloxacin with Simultaneous Hydrogen Production. *Chem. Eng. J.* **2020**, *382*, 122394. [CrossRef]

70. Laurent, S.; Forge, D.; Port, M.; Roch, A.; Robic, C.; vander Elst, L.; Muller, R.N. Magnetic Iron Oxide Nanoparticles: Synthesis, Stabilization, Vectorization, Physicochemical Characterizations and Biological Applications. *Chem. Rev.* **2008**, *108*, 2064–2110. [CrossRef]

71. Alfredo Reyes Villegas, V.; Isaías De León Ramírez, J.; Hernandez Guevara, E.; Perez Sicairos, S.; Angelica Hurtado Ayala, L.; Landeros Sanchez, B. Synthesis and Characterization of Magnetite Nanoparticles for Photocatalysis of Nitrobenzene. *J. Saudi Chem. Soc.* **2020**, *24*, 223–235. [CrossRef]

72. Peralta, M.E.; Nisticò, R.; Franzoso, F.; Magnacca, G.; Fernandez, L.; Parolo, M.E.; León, E.G.; Carlos, L. Highly Efficient Removal of Heavy Metals from Waters by Magnetic Chitosan-Based Composite. *Adsorption* **2019**, *25*, 1337–1347. [CrossRef]

73. Yang, X.; Cui, H.; Li, Y.; Qin, J.; Zhang, R.; Tang, H. Fabrication of Ag_3PO_4-Graphene Composites with Highly Efficient and Stable Visible Light Photocatalytic Performance. *ACS Catal.* **2013**, *3*, 363–369. [CrossRef]

74. Yang, Z.-M.; Huang, G.-F.; Huang, W.-Q.; Wei, J.-M.; Yan, X.-G.; Liu, Y.-Y.; Jiao, C.; Wan, Z.; Pan, A. Novel Ag_3PO_4/CeO_2 Composite with High Efficiency and Stability for Photocatalytic Applications. *J. Mater. Chem. A* **2014**, *2*, 1750–1756. [CrossRef]

75. Yin, H.; Cao, Y.; Fan, T.; Zhang, M.; Yao, J.; Li, P.; Chen, S.; Liu, X. In Situ Synthesis of Ag_3PO_4/C_3N_5 Z-Scheme Heterojunctions with Enhanced Visible-Light-Responsive Photocatalytic Performance for Antibiotics Removal. *Sci. Total Environ.* **2021**, *754*, 141926. [CrossRef]

76. Cao, W.; An, Y.; Chen, L.; Qi, Z. Visible-Light-Driven Ag_2MoO_4/Ag_3PO_4 Composites with Enhanced Photocatalytic Activity. *J. Alloys Compd.* **2017**, *701*, 350–357. [CrossRef]

77. Beydoun, D.; Amal, R.; Low, G.K.-C.; McEvoy, S. Novel Photocatalyst: Titania-Coated Magnetite. Activity and Photodissolution. *J. Phys. Chem. B* **2000**, *104*, 4387–4396. [CrossRef]

78. Taheri, M.E.; Petala, A.; Frontistis, Z.; Mantzavinos, D.; Kondarides, D.I. Fast Photocatalytic Degradation of Bisphenol A by Ag_3PO_4/TiO_2 Composites under Solar Radiation. *Catal. Today* **2017**, *280*, 99–107. [CrossRef]

79. Du, Y.E.; Li, W.; Bai, Y.; Huangfu, Z.; Wang, W.; Chai, R.; Chen, C.; Yang, X.; Feng, Q. Facile Synthesis of TiO_2/Ag_3PO_4 composites with Co-Exposed High-Energy Facets for Efficient Photodegradation of Rhodamine B Solution under Visible Light Irradiation. *RSC Adv.* **2020**, *10*, 24555–24569. [CrossRef]

80. Yao, W.; Zhang, B.; Huang, C.; Ma, C.; Song, X.; Xu, Q. Synthesis and Characterization of High Efficiency and Stable Ag_3PO_4/TiO_2 Visible Light Photocatalyst for the Degradation of Methylene Blue and Rhodamine B Solutions. *J. Mater. Chem.* **2012**, *22*, 4050–4055. [CrossRef]

81. Guo, R.; Xia, X.; Zhang, X.; Li, B.; Zhang, H.; Cheng, X.; Xie, M.; Cheng, Q. Construction of Ag_3PO_4/TiO_2 Nano-Tube Arrays Photoelectrode and Its Enhanced Visible Light Driven Photocatalytic Decomposition of Diclofenac. *Sep. Purif. Technol.* **2018**, *200*, 44–50. [CrossRef]

82. Woo, K.J.; Hye, C.K.; Ki, W.K.; Shin, S.; So, H.K.; Yong, H.P. Antibacterial Activity and Mechanism of Action of the Silver Ion in *Staphylococcus aureus* and *Escherichia coli*. *Appl. Environ. Microbiol.* **2008**, *74*, 2171–2178. [CrossRef]

83. Armstrong, D.A.; Huie, R.E.; Koppenol, W.H.; Lymar, S.V.; Merenyi, G.; Neta, P.; Ruscic, B.; Stanbury, D.M.; Steenken, S.; Wardman, P. Standard Electrode Potentials Involving Radicals in Aqueous Solution: Inorganic Radicals (IUPAC Technical Report). *Pure Appl. Chem.* **2015**, *87*, 1139–1150. [CrossRef]

84. Hewer, T.L.R.; Machado, B.C.; Freire, R.S.; Guardani, R. Ag_3PO_4 Sunlight-Induced Photocatalyst for Degradation of Phenol. *RSC Adv.* **2014**, *4*, 34674–34680. [CrossRef]

85. Rupa, A.V.; Manikandan, D.; Divakar, D.; Sivakumar, T. Effect of Deposition of Ag on TiO_2 Nanoparticles on the Photodegradation of Reactive Yellow-17. *J. Hazard. Mater.* **2007**, *147*, 906–913. [CrossRef]

86. Tortella, G.R.; Rubilar, O.; Durán, N.; Diez, M.C.; Martínez, M.; Parada, J.; Seabra, A.B. Silver Nanoparticles: Toxicity in Model Organisms as an Overview of Its Hazard for Human Health and the Environment. *J. Hazard. Mater.* **2020**, *390*, 121974. [CrossRef]

87. Beer, C.; Foldbjerg, R.; Hayashi, Y.; Sutherland, D.S.; Autrup, H. Toxicity of Silver Nanoparticles-Nanoparticle or Silver Ion? *Toxicol. Lett.* **2012**, *208*, 286–292. [CrossRef]

88. World Health Organization. *Silver in Drinking-Water Background Document for Development of WHO Guidelines for Drinking-Water Quality*; World Health Organization: Geneva, Switzerland, 2021.